Materialia 20 (2021) 101223

Contents lists available at ScienceDirect

Materialia

journal homepage: www.elsevier.com/locate/mtla

Full Length Article

Evolution of strength properties and defect sub-structure of the hypoeutectic A319.0 alloy irradiated by a pulsed electron beam and fractured under tensile stress

D.V. Zaguliaev[a,*], Yu.F. Ivanov[b], A.A. Klopotov[b], A.M. Ustinov[b], V.V. Shlyarov[a], D.F. Yakupov[a]

[a] Siberian State Industrial University, 654007 Novokuznetsk, Russia
[b] Institute of High-Current Electronics, 634055 Tomsk, Russia

ARTICLE INFO

Keywords:
Pulsed electron beam
Tensile stress
Aluminum alloy
Microstructure

ABSTRACT

The paper intends to investigate strength and plasticity properties and defect sub-structure of the hypoeutectic A319.0 alloy irradiated by a pulsed electron beam. The study has established and the revealed extinction contours point out that the irradiation of the A319.0 alloy by a pulsed electron beam brings about the formation of an up to 100 μm thick surface layer in the elastic-stressed state. The structure of the modified layer comprises nano-dimensional non-equiaxed cells. The reason for the non-equiaxity in a cellular structure is suggested to be the irregular heat removal from the surface of modification. X-ray microspectroscopy has found out that high-speed crystallization cells are formed by an aluminum-based solid solution and separated with thin layers, which are enriched mainly by silicon atoms and, to a smaller degree, by atoms of magnesium, iron and copper.

The data obtained in the mechanical testing suggest that the irradiation was carried out in the following conditions: 50 J/cm^2 and 50 μs results in the simultaneous enhancement of strength (by 22%) and plasticity (by 44%) properties of the A319.0 alloy – these are the best positive values in the set of conducted experiments. The study on A319.0 alloy samples irradiated and fractured under the tensile stress has highlighted that their fracture is dominated by the mechanism of intercrystalline quasi-brittle rupture caused by forming lengthy thin layers of the second phase along the boundaries of high-speed crystallization cells.

1. Introduction

The majority of present-day engineering materials is manufactured coated or with strengthened effective surfaces [1–3]. The properties of sub-surface layers are of high importance for maintaining the performance characteristics of engineering materials. Unfortunately, the surface properties of aluminum alloys sometimes fail to meet the actual industrial requirements, e.g. Al-Si alloys used in the automotive industry are not always can satisfy the required tribological and thermomechanical characteristics for engine blocks [4]. At the same time, it is important that engineering materials would be deformable and able to withstand mechanical loads without structural failures during the entire lifetime, Therefore, of high concern is the research aimed at finding new methods to increase the strength of aluminum alloys via modifying their surface [5–7].

Recent review of literature has shown an increased interest to the treatment by high-current pulsed electron beams to impart unique mechanical and technological properties of such materials as high-entropy alloys [8], magnesium alloys [9,10], steels [11,12], alloys of the Zn –Cu system [13] and aluminum alloys [14,15].

Gao [16] thoroughly examined the effect of high current pulse-beam treatment induced by the shock wave nano-crystallization on mechanical properties of the hypereutectic Al-15Si alloy. The study on mechanical properties of the Al-15Si alloy before and after high-current pulsed beam treatment demonstrated that the tensile strength of the irradiated Al-15Si alloy increased by ≈ 41.4% (from 138.8 MPa in an untreated sample to 196.2 MPa in a modified sample).

A number of scientists [17] conducted the research with the purpose to investigate a role of the beam current force for microstructure, phase composition, disorientation of grain boundaries and mechanical characteristics of the Ti-47Al-2Cr-2Nb alloy fabricated via selective electron-beam melting. The results showed that an increasing beam current modified a finely dispersed microstructure with an average grain of 3.02 μm into a structure with middle-sized grains of 6.28 μm. The ultimate compression strength of the irradiated TiAl alloy decreased from 2930.95 MPa to 2456.82 MPa and the deformation (δ) – from 34.82 to 27.44%

* Corresponding author at: Siberian State Industrial University, 654007 Novokuznetsk, Russian Federation
E-mail address: zagulyaev_dv@physics.sibsiu.ru (D.V. Zaguliaev).

https://doi.org/10.1016/j.mtla.2021.101223
Received 24 June 2021; Accepted 12 September 2021
Available online 15 September 2021

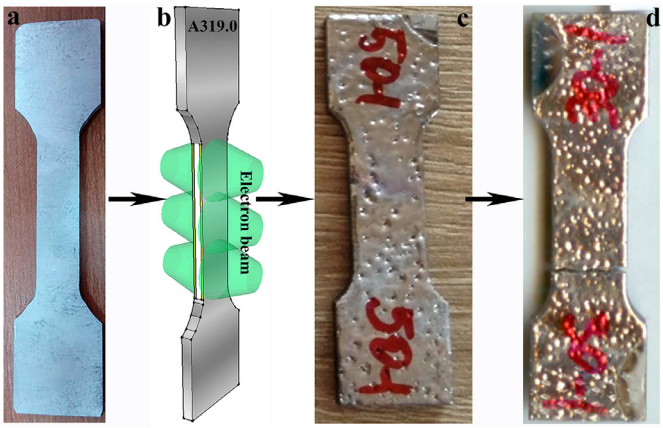

Fig. 1. A general view of samples for testing (a), a diagram of electron-beam irradiation (b), a general view of samples irradiated by an electron beam (c) and subjected to the uniaxial tension until failure (d).

upon increasing the beam current from 4.5 to 8.5 mA. The worsening of strength properties under compression was related to the increase of a grain size.

Liu Y.R. et al. [18,19] established that the Mg-4Sm-2Al-0.5Mn alloy exhibited the best corrosion resistance under the high-current pulsed electron beam treatment irrespectively to a pulse number mainly because of the homogenous microstructure and less defective composition of the surface layer on completion of repetitive melting and rapid solidification.

The focus of study [20] was the evolution of microstructure and properties in the aluminum 6061 alloy irradiated by a pulsed electron beam generated by a pseudo-spark discharge. The pseudo-spark discharge is an intermediate low-pressure discharge recognized to be a highly efficient electron beam source with a rapidly growing current, high power density, a short-time pulse and diameter of a self-focusing beam. Xiao-Tong Cao et al. found that a liquid surface layer was formed in the material subjected to the pseudo-spark pulsed electron-beam irradiation, furthermore, a higher value of voltage brings about the "big crater" morphology. The more homogenized distribution of elements on the surface and reduction of impurities on the molten layer after a series of pulsed electron-beam treatments could enhance mechanical properties of the sample surface and the corrosion resistance of the alloy [20].

In studies [21,22] hypereutectic Ai-Si alloys were irradiated by a high-current pulsed electron beam. It was reported that the high-current pulsed electron beam treatment enlarged and displaced the Al and Si diffraction peaks. Aluminum lattice parameters decreased due to the formation of an oversaturated aluminum solid solution in the liquid layer. The wear resistance of the treated alloy was improved by 9 times; that could be related to the formation of meta-stable structures.

Studies [23–25] pointed out that the effect of a pulsed electron beam on the materials surface improved their anticorrosion properties. It was demonstrated that the rapid solidification inevitably caused the significant refinement of grains, even to nano-dimensional or submicron range [26–28].

All of the studies reviewed here support the hypothesis that electron-beam treatment is a promising method to modify the structure and properties of metallic materials. The outlined reasons emphasize the need of a proposed study since it aims at revealing and analyzing variation regularities of such characteristics as ultimate strength, yield strength, relative residual elongation at fracture and percent reduction in area at fracture, as well as element and phase composition, defect sub-structure of the hypoeutectic A319.0 alloy irradiated by an electron beam and fractured under tensile stress.

Since aluminum alloys, the A319.0 alloy in particular, represent one of the most widespread materials, the assessment of their properties in terms of their operation conditions and diverse external energy effects

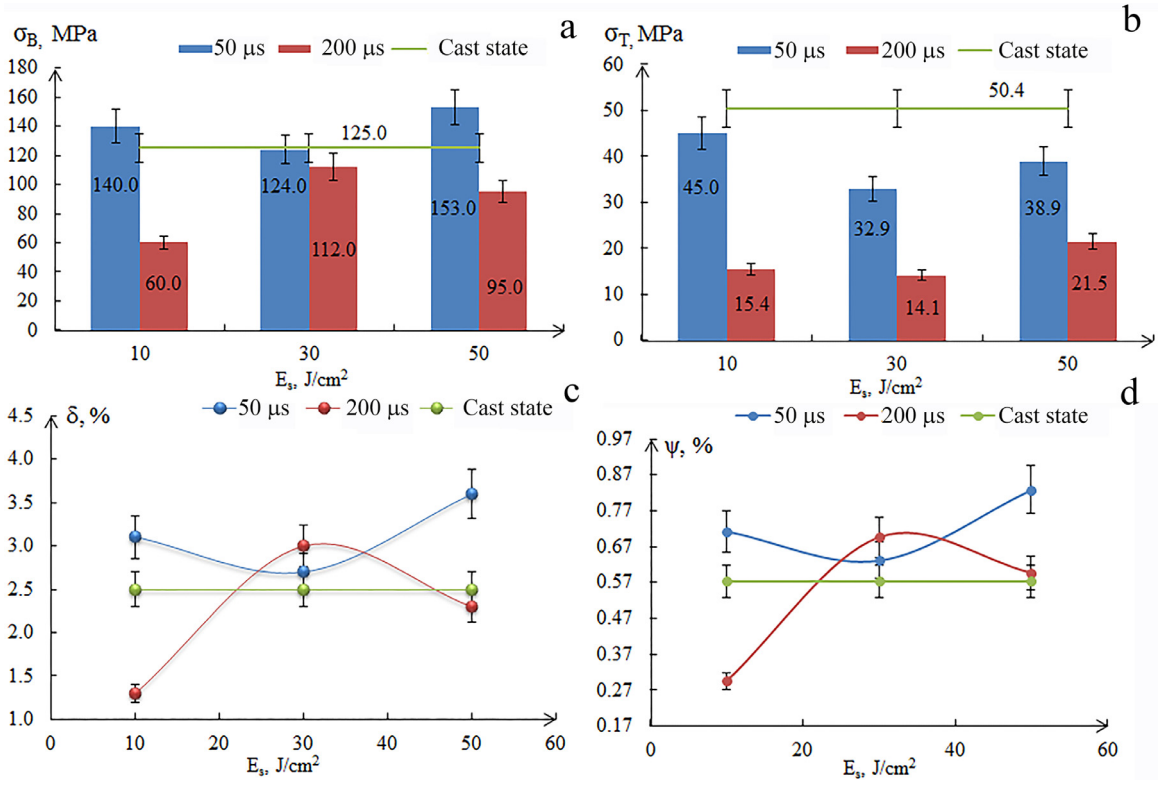

Fig. 2. Average ultimate strength (a), yield strength (b), relative residual elongation at fracture (c) and percent reduction in area at fracture (d) as functions on the energy density of an electron beam at a pulse time of an electron beam of 50 and 200 μs for the A319.0 alloy.

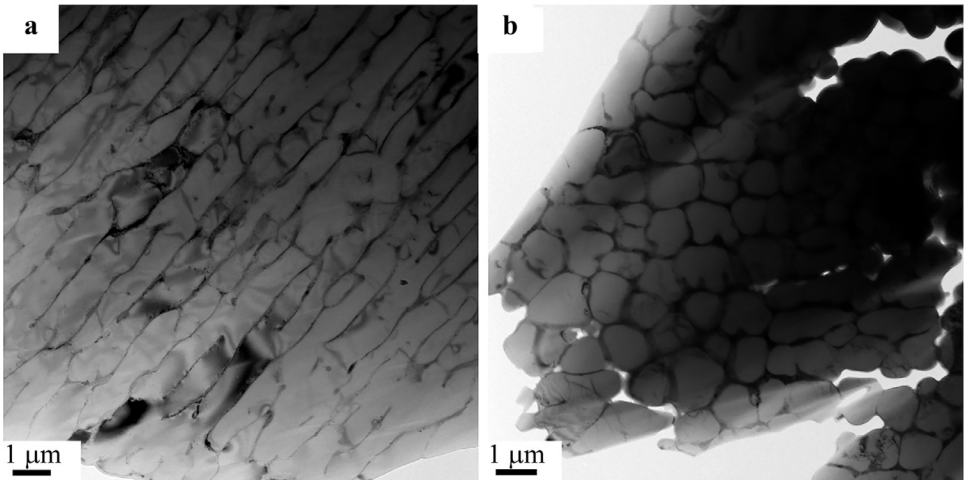

Fig. 3. Electron-microscopy micrograph of the structure in the A319.0 alloy irradiated by a pulsed electron beam; the view was obtained by a STEM-based analysis of foils placed perpendicular (a) and parallel (b) to the irradiated surface.

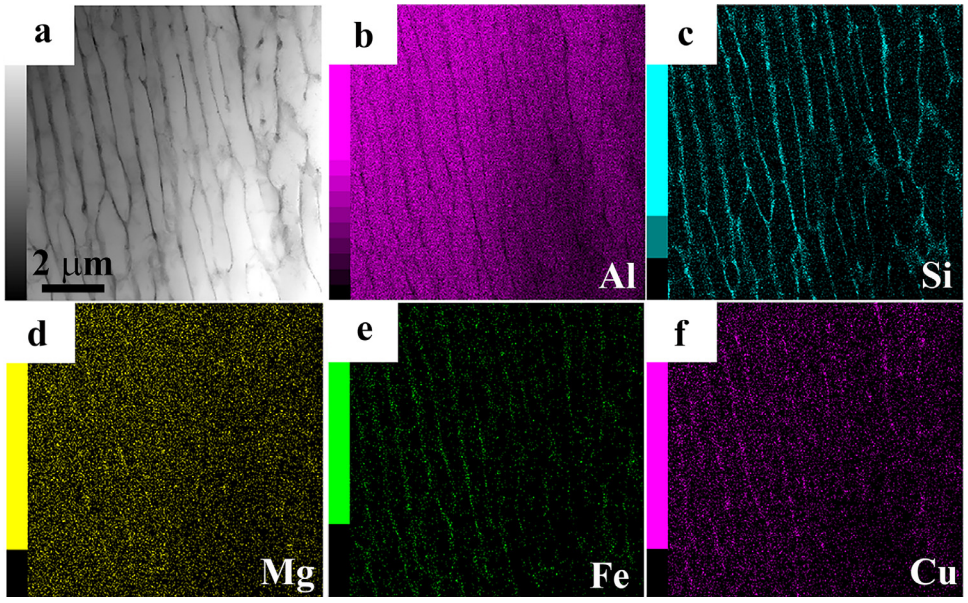

Fig. 4. Electron-microscopy micrograph of a foil area obtained in a STEM-based analysis (a); images (b-f) were obtained in the characteristic X-ray emission of Al, Si, Mg, Fe and Cu atoms.

becomes an interesting issue both in research [29–31] and practical [32,33] perspectives.

2. Methods and materials

The study was conducted on the general-purpose hypoeutectic cast A319.0 alloy, which is widely applied in different industries [34]. The tensile testing of the alloy was performed on plane proportional samples fabricated in the form of two-sided blades according to the ISO 6892-1:2016 Metallic materials – Tensile testing – Part 1: Method of test at room temperature [35]. Samples for testing were prepared from a solid ingot via electric discharge cutting. Fabricated samples were grinded and polished using diamond pastes with various dispersion grades. The sizes of samples ready for testing were as follows: the thickness – 2.3 mm; the width – 9.1 mm; a length of an effective surface – 16.0 mm (fig. 1a). Polished samples were divided into two sets. The first set remained untreated. The effective surface of samples in the second set was irradiated by a pulsed electron beam from both sides (fig. 1b) in vacuum using a laboratory unit "SOLO" [36]. The parameters of an electron beam were set for all impact modes: the energy of accelerated electrons – 17 keV, a number of pulses – 3, a repetition rate of pulses – 0.3 s^{-1}; the pressure of a residual gas (argon) in the processing chamber of the unit $2 \cdot 10^{-2}$ Pa. The energy density of an electron beam and a time of

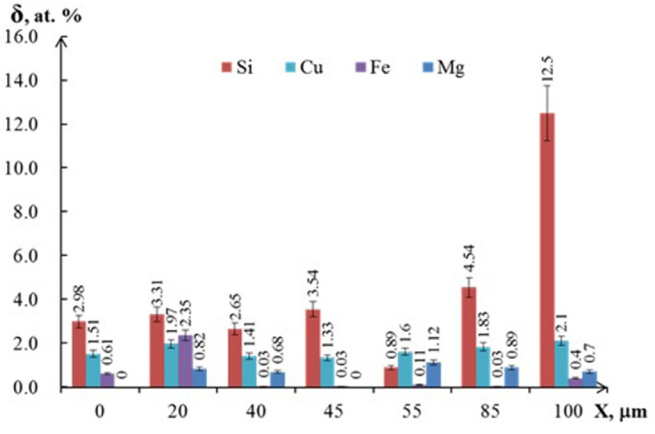

Fig. 5. Concentration of alloying elements vs. distance to surface of the A319.0 alloy subjected to pulsed electron beam.

pulses were varied in the range from 10 to 50 J/cm^2 and from 50 to 200 μs, respectively. A general view of modified samples is given in fig. 1c.

The mechanical testing of the A319.0 alloy represented the uniaxial tension until failure using a unit "INSTRON 3386" at a constant speed of

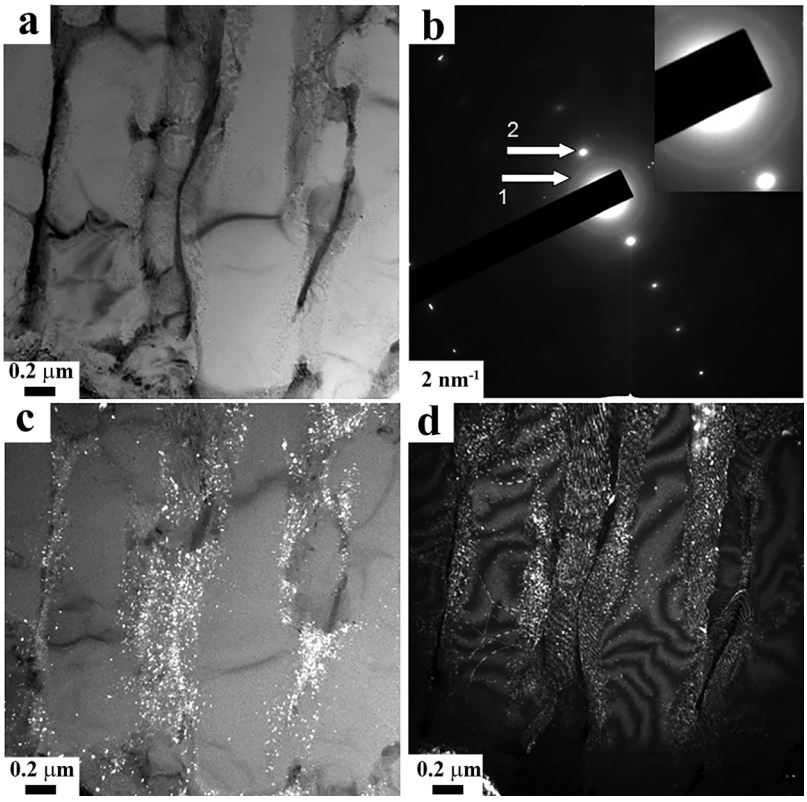

Fig. 6. Electron-microscopy micrograph of the surface layer structure of the A319.0 alloy irradiated by a pulsed electron beam; a – bright field; b – electron diffraction micro-pattern; c, d – dark-field images obtained in reflexes [111]Si (c) and [111]Al + [220] Si (d). The arrows (b) indicate reflexes: 1 – for (c) and 2 – for (d).

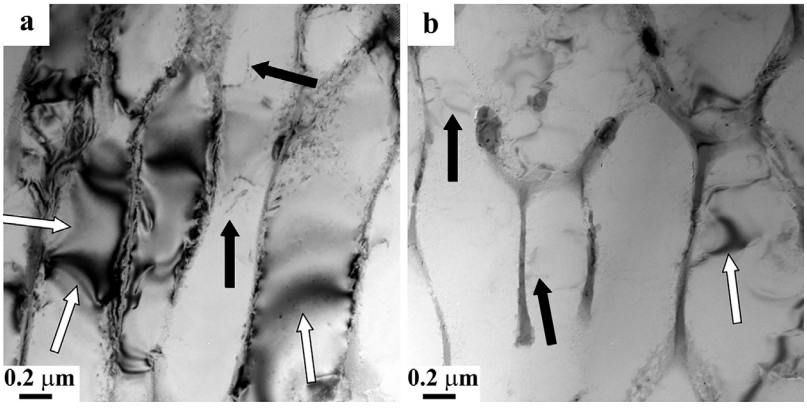

Fig. 7. Electron-microscopy micrograph of the structure in the A319.0 alloy irradiated by a pulsed electron beam; the white arrows indicate bend contours of extinction. Black arrows indicate of dislocations.

1.25 mm/min, at least 3 samples were tested for each irradiation mode. A general view of fractured samples of the hypoeutectic A319.0 alloy is presented in fig. 1d.

The element and phase composition, defect sub-structure state and fracture surface were investigated with the help of a scanning electron microscope Philips SEM-515 equipped with an energy dispersion detector for X-ray microspectroscopy EDAX ECON IV, which makes it possible to examine the occurrence, concentration and distribution of metallic materials in a sample, and a transmission electron microscope JEM 2100F, JEOL, using the method of annular dark and bright field imaging, as well as a scanning mode (STEM). When carrying out a STEM analysis, the electron beam is focused into a 0.05–0.2 nm thin spot, further the beam scans a material of interest in the raster lighting system. STEM has the potential to visualize a nanostructured material surface with high spatial resolution and study the distribution of elements in the scanned zone. Foils for exploring the structure and phase state of the material with the methods of transmission electron microscopy in the diffraction mode were prepared via ion beam sputtering of plates, which were cut perpendicular to the irradiated surface of a sample using the spark discharge method. A cutting mode was set precisely to avoid unnecessary deformation and therefore have no effect on the structure of a sample.

3. Results and discussion

3.1. Tension-induced plastic deformation of the A319.0 alloy in the as cast state and irradiated by a pulsed electron beam

The mechanical testing represented the uniaxial tension and simultaneous recording the stress-strain curve both for the as cast A319.0 alloy and the material modified by an electron beam in different modes. Such characteristics as ultimate strength, yield strength, relative residual elongation at fracture and percent reduction in area at fracture were determined according to data of the stress-strain curves. Using values of these characteristics, their average values were plotted as functions of the electron beam energy density and a pulse time (fig. 2).

From the data shown in fig. 2a it is apparent that in the irradiation mode: 10 J/cm^2 and 50 J/cm^2, 50 μs, the ultimate tensile strength in-

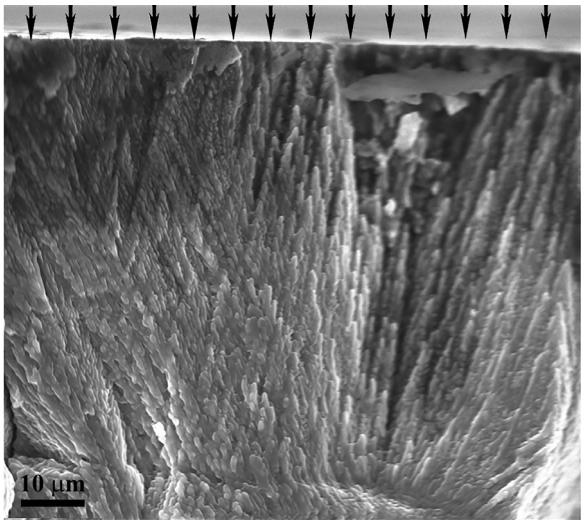

Fig. 8. Electron-microscopy micrograph of the fracture surface structure in the A319.0 alloy irradiated by a pulsed electron beam; SEM. The arrows indicate the irradiated surface.

creases by 15 MPa and 28 MPa, respectively, i.e. by 12 % and 22.4 %, in comparison with the as cast alloy. However, it is noteworthy that the correlation between yield strength and energy density of an electron beam hardly demonstrates this behavior (fig. 2b). The electron-beam treatment causes a decrease in yield strength irrespectively to irradiation modes.

The functions of relative residual elongation and percent reduction in area at fracture on the energy density of an electron beam (figs. 2 c, d) demonstrate that these parameters tend to significant changes for non-overlapping confidence intervals in irradiation modes: 10 J/cm^2, 200 μs and 50 J/cm^2, 50 μs. Moreover, both parameters decline in the first presented mode but they grow in the second presented mode. An increase in the relative residual elongation and contraction at fracture points indirectly testifies at increase in plastic properties of the material.

Therefore, it can be stated that the irradiation mode: 50 J/cm^2, 50 μs, is associated to a simultaneous increase of strength and plasticity in the A319.0 alloy. The identified fact is of interest for further research works to carry out using methods of the present-day physical materials science with the purpose to reveal transformations in the structure and their relation to the detected changes of properties. The latter were done in the work.

3.2. Study on the defect sub-structure, element and phase composition of the hypoeutectic A319.0 alloy irradiated by a pulsed electron beam

The transmission electron microscopy pointed out that the irradiation of the A319.0 alloy by a pulsed electron beam resulted in the high-speed melting of an up to 100 μm thick surface layer. The subsequent high-speed crystallization in the surface layer brings about the formation of a submicro-nanocrystalline structure; its typical view is shown in fig. 3. From the data in fig. 3 it is apparent that crystallization cells are non-equiaxed [37,38]. The longitudinal axis of cells is oriented towards the heat removal, i.e. perpendicular to the irradiation surface (fig. 3 a). The cells are roundish in the cross-section (fig. 3 b). Therefore, it is likely that high-crystallization cells possess a cylindrical form with a longitudinal axis oriented towards the heat removal.

The distribution of alloying elements in the surface layer subjected to the high-speed crystallization was studied using the mapping method (STEM EOX). An important outcome to emerge from the study is that high-speed crystallization cells are formed by an aluminum-based solid solution (fig. 4 a, b). The cells are separated by thin layers to be enriched mainly with atoms of silicon and, to a smaller degree, with atoms of magnesium, iron and copper (fig. 4 c-f). Importantly, atoms of all alloying element except for silicon are found in an aluminum-based solid solution (the volume of cells).

The distribution of alloying elements through the material thickness in the layer after high-speed melting to result from the irradiation of the A319.0 alloy by a pulsed electron beam is shown in fig. 5. As seen, the high-speed crystallization is related to the formation of a surface layer with alloying elements distributed in a quasi-homogenous way. The distribution heterogeneity of alloying elements intensifies with a distance from the surface. It is especially typical for silicon, which is a major alloying element in the compound.

The phase composition of the modified layer was explored using the methods of electron microscopy in the diffraction mode, dark-field imaging and indexing of electron diffraction patterns [39,40]. The research outcomes highlight that high-speed crystallization cells are formed by an aluminum-based solid solution (fig. 6 d). On the boundaries of cells there are mainly spherical particles of silicon, their sizes vary in the range of 10-20 nm (fig. 6 c, d). A particular attention should be paid to

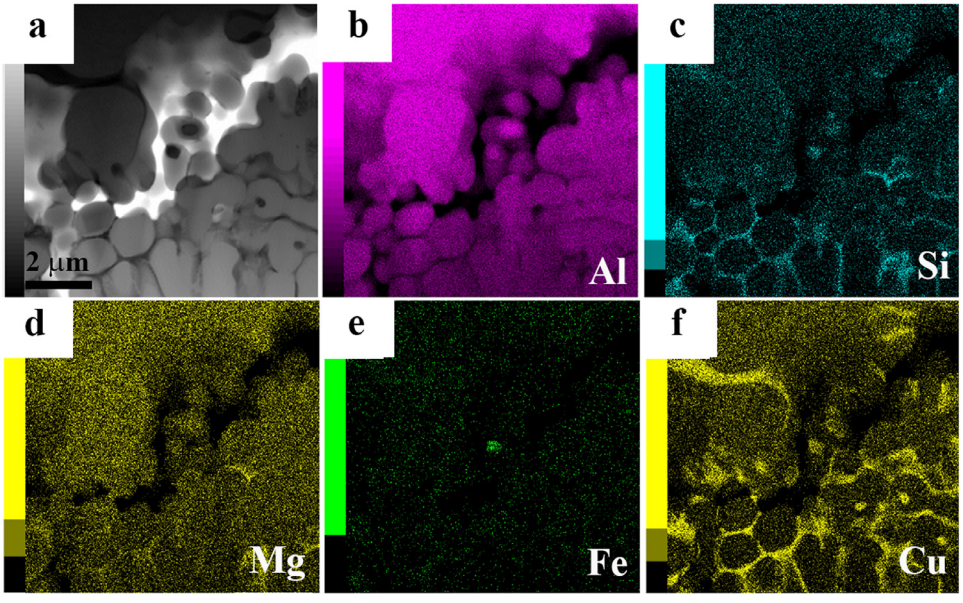

Fig. 9. Electron-microscopy micrograph of a foil section prepared from the A319.0 alloy fractured under the uniaxial tension of plane samples obtained in a STEM-based analysis (a); images (b-f) were made in the characteristic X-ray emission of Al, Si, Mg, Fe, and Cu atoms, respectively.

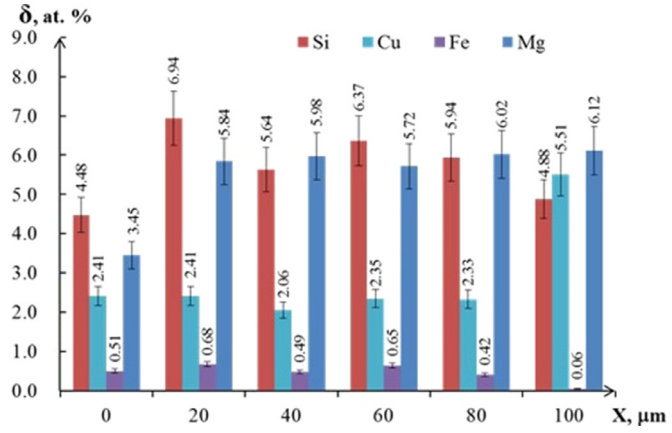

Fig. 10. Concentration of alloying elements vs. distance to the surface irradiated by a pulsed electron beam in A319.0 alloy samples fractured under tension.

narrow diffusion rings in the electron diffraction micro-pattern (fig. 6 b, an insert) in the area with silicon reflexes. This fact may point at the formation of a silicon phase, both in crystalline and amorphous states.

The defect sub-structure of crystallization cells is formed by dislocations. The dislocations are chaotically distributed in the volume of cells (fig. 7 a). The scalar density of dislocations determined by the random linear intercept method [39] varies in the range of (3-5)•10^9 cm^{-2}. The surface layer of a sample irradiated by a pulsed electron beam is in the elastic-stressed state. This is demonstrated by the extinction contours detected when examining the material by the method of thin foils (fig. 7, the contours indicated by the arrows). The sources of shear and torsion in the crystal lattice of the alloy are boundaries between cells (fig. 7 a) and second-phase particles found on the boundaries between cells and in the volume of cells (fig. 7 b).

Therefore, the irradiation of the A319.0 alloy by a pulsed electron beam induces the melting of a relatively thin surface layer. The subsequent high-speed crystallization is related to the formation of a submicro-nanocrystalline multiphase structure with quasi-homogenously distributed alloying elements. The surface layer in the alloy irradiated by a pulsed electron beam is in the elastic-stress state as demonstrated by the detected bend extinction contours.

3.3. Evolution of the defect sub-structure, element and phase composition in the hypoeutectic A319.0 alloy irradiated by a pulsed electron beam and fractured under tension

The fracturing of A319.0 alloy samples under the uniaxial tension on an example of plane proportional samples with the effective surface irradiated by a pulsed electron beam (50 J/cm^2, 50 μs) from both sides causes significant transformations in the material structure. The research into the element and phase composition, the defect sub-structure state of deformed samples was carried out via analyzing foils, which were prepared in the ion thinning of plates cut as close as possible to the fracture surface and at different depths below it.

The SEM-based study on the fracture surface (fig. 8) points out that the fracture of a layer irradiated by a pulsed electron beam represents the sliding of micro-cracks along crystallization cell boundaries, i.e. an intercrystalline (inter-grain) rupture is formed. Under intercrystalline rupture fracture is dominated by crack propagation mainly along grain boundaries their lower strength in comparison with the transgranular portions of the grains. Such factors as segregation of impurities on grain boundaries, formation of brittle inter-grain thin layers of intermediate phases, adsorption-related strength reduction and decrease (cold brittleness) or increase (hot brittleness) of temperature further the intercrystalline rupture. It is obvious and the findings of the X-ray microspectroscopy presented in fig. 9 demonstrate that the key reason for the intercrystalline rupture in the material under study is the enrichment of cell boundaries with impurity atoms and atoms of alloying elements, as well as the formation of second-phase inclusions.

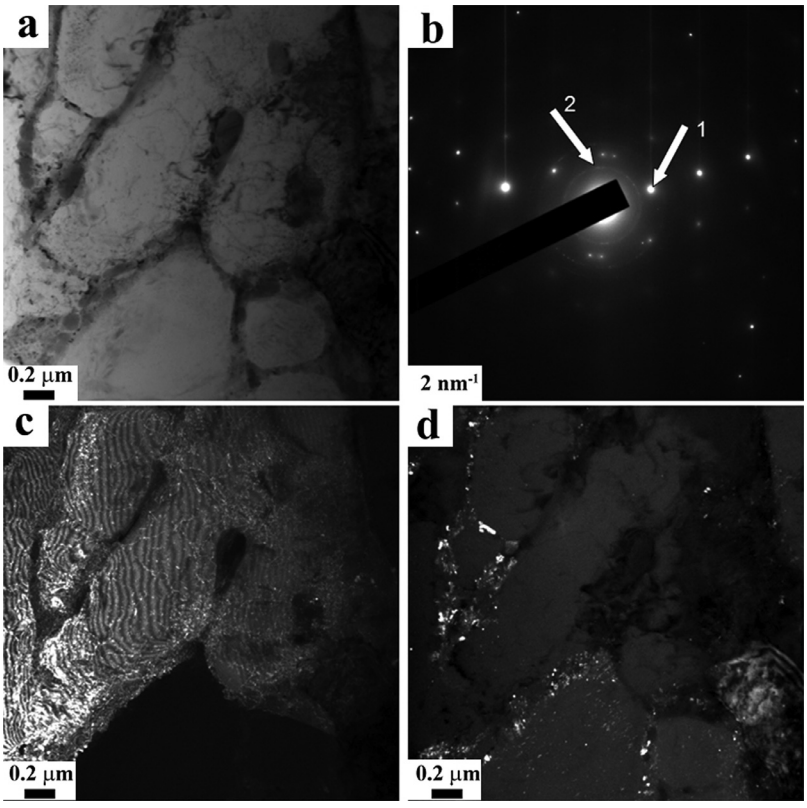

Fig. 11. Electron-microscopy micrograph of the surface layer structure in the A319.0 alloy irradiated by a pulsed electron beam and fractured under tension; a – bright field; b – electron diffraction micro-pattern; c, d – dark-field images obtained in reflexes [111]Al (c) and [111]Si (d). The arrows (b) indicate reflexes: 1 – for (c) and 2 – for (d).

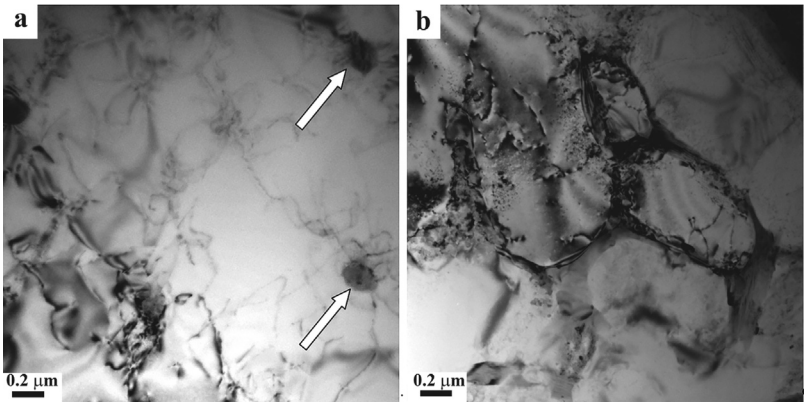

Fig. 12. Electron-microscopy micrograph of the A319.0 alloy structure irradiated by a pulsed electron beam and fractured under tension. The arrows (a) indicate particles, around which dislocation clusters are formed.

It should be noted that the distribution of elements within the boundaries of crystallization cells hardly changes under the intercrystalline rupture of the alloy (fig. 10.); it remains quasi-homogenous, however, with certain specifics. Comparing fig. 10 and fig. 5, a conclusion is made that the concentration of all alloying elements on the surface is significantly higher in surface fractured samples (Si, Mg, Fe, Cu).

Under the intercrystalline (quasi-brittle) rupture there is a slight deformation in the areas close to the boundaries and in the volume of cells (grains). The study on the fracture zone in the A319.0 alloy detected some remaining nano-dimensional thin layers of silicon particles along the cell boundaries (fig. 11).

A dislocation sub-structure in the form of randomly distributed dislocations and those forming clusters is formed in the volume of crystallization cells (fig. 12). The centers with forming dislocations clusters represent rather frequent second-phase (Si) particles (fig. 12 (a), indicated by the arrow). The scalar density of dislocations is determined to be $2.1 \cdot 10^{10}$ cm^{-2} that is almost by an order of magnitude higher than that of dislocations in the cell structure before the deformation of samples.

To sum up, despite a submicro-nanocrystalline structure forming when irradiating the A319.0 alloy by a pulsed electron beam strength and plasticity properties of the material exhibit only an insignificant increase under the uniaxial tension of plane samples because of lengthy second-phase thin layers developing along the high-speed crystallization cells and initiating the intercrystalline quasi-brittle fracturing.

4. Conclusion

The tensile testing of A319.0 alloy samples modified by an electron beam revealed that the irradiation mode: 50 J/cm^2, 50 μs was related to a simultaneous increase of strength and plasticity properties by 22.4 and 44.0 %, respectively – these data represented the highest measurement in the set of conducted experiments. The detected changes contributed to the selection of the given irradiation mode for the research into the structure and its correlation with the detected transformations of properties.

The study on the microstructure demonstrated that the irradiation of the A319.0 alloy by a pulsed electron beam (17 keV, 50 J/cm^2, 50 μs, 3 pulses, 0.3 s^{-1}) leads to the melting of a relatively thin (up to 100 μm) surface layer. The subsequent high-speed crystallization brings about the formation of a submicro-nanocrystalline multiphase structure with quasi-homogenously distributed alloying elements and particles of the second phase.

Scanning and transmission electron microscopy methods were used to explore the fracture surface, structure and chemical composition in irradiated and fractured samples of the A319.0 alloy. The research findings demonstrated that the fracture is dominated by the mechanism of intercrystalline quasi-brittle rupture induced by lengthy thin layers of the second phase (Si) forming along the boundaries of high-speed crystallization cells; this fact explains an insignificant increase of strength and plasticity properties of the alloy even if there is a submicro-nanocrystalline multiphase structure in the surface layer. The quasi-homogenous distribution of chemical elements remains, however, their concentration is significantly higher than in non-fractured but irradiated samples.

Declaration of Competing Interest

The authors declare that they have no known competing financial interests or personal relationships that could have appeared to influence the work reported in this paper.

Acknowledgments

The study was supported by the Russian Science Foundation (project No. 19-79-10059).

References

[1] A. Krishnan, A.V Krishnan, A. Ajith, S.M.A. Shibli, Influence of materials and fabrication strategies in tailoring the anticorrosive property of superhydrophobic coatings, Surfaces and Interfaces. 25 (2021) 101238, doi:10.1016/j.surfin.2021.101238.
[2] W. Tillmann, N.F. Lopes Dias, D. Stangier, C. Schaak, S. Höges, Coatability of diamond-like carbon on 316L stainless steel printed by binder jetting, Addit. Manuf. 44 (2021) 102064, doi:10.1016/j.addma.2021.102064.
[3] S. Lu, J. Zhou, L. Wang, J. Liang, Influence of MoSi2 on the microstructure and elevated-temperature wear properties of Inconel 718 coating fabricated by laser cladding, Surf. Coatings Technol. 424 (2021) 127665, doi:10.1016/j.surfcoat.2021.127665.
[4] M. Javidani, D. Larouche, Application of cast Al–Si alloys in internal combustion engine components, Int. Mater. Rev. 59 (2014) 132–158, doi:10.1179/1743280413Y.0000000027.
[5] G.K. Badhotiya, A. Saini, D. Singh, A.S. Chauhan, Oxime-modified aluminum (III) isopropoxide: A promising sol-gel precursor coating to improve mechanical strength of an aluminum alloy, Mater, Today Proc. (2021), doi:10.1016/j.matpr.2021.01.332.
[6] V.V Bryukhovetsky, V.F. KLepikov, V.V Lytvynenko, D.E. Myla, V.P. Poyda, A.V Poyda, V.T. Uvarov, Y.F. Lonin, A.G. Ponomarev, The features of the structural state and phase composition of the surface layer of aluminum alloy Al-Mg-Cu-Zn-Zr irradiated by the high current electron beam, Nucl. Instruments Methods Phys. Res. Sect. B Beam Interact. with Mater. Atoms. 499 (2021) 25–31, doi:10.1016/j.nimb.2021.02.011.
[7] A. Matei, O. Tutunaru, V. Tucureanu, Surface pre-treatment of aluminum alloys for the deposition of composite materials, Mater. Sci. Eng. B. 263 (2021) 114874, doi:10.1016/j.mseb.2020.114874.
[8] P. Lyu, T. Peng, Y. Miao, Z. Liu, Q. Gao, C. Zhang, Y. Jin, Q. Guan, J. Cai, Microstructure and properties of CoCrFeNiMo0.2 high-entropy alloy enhanced by high-current pulsed electron beam, Surf. Coatings Technol. 410 (2021) 126911, doi:10.1016/j.surfcoat.2021.126911.
[9] T.C. Zhang, K.M. Zhang, J.X. Zou, P. Yan, H.Y. Yang, L.X. Song, X. Zhang, Surface microstructure and property modifications in a Mg-8Gd-3Y-0.5Zr magnesium alloy treated by high current pulsed electron beam, J. Alloys Compd. 788 (2019) 231–239, doi:10.1016/j.jallcom.2019.02.130.
[10] F. Morini, M. Bestetti, S. Franz, A. Vicenzo, A. Markov, E. Yakovlev, Surface properties modification of magnesium alloys by low energy high current pulsed electron beam, Surf. Coatings Technol. 420 (2021) 127351, doi:10.1016/j.surfcoat.2021.127351.

[11] Y. Samih, G. Marcos, N. Stein, N. Allain, E. Fleury, C. Dong, T. Grosdidier, Microstructure modifications and associated hardness and corrosion improvements in the AISI 420 martensitic stainless steel treated by high current pulsed electron beam (HCPEB), Surf. Coatings Technol. 259 (2014) 737–745, doi:10.1016/j.surfcoat.2014.09.065.
[12] J. Zou, T. Grosdidier, K. Zhang, C. Dong, Mechanisms of nanostructure and metastable phase formations in the surface melted layers of a HCPEB-treated D2 steel, Acta Mater 54 (2006) 5409–5419, doi:10.1016/j.actamat.2006.05.053.
[13] L.X. Song, K.M. Zhang, J.X. Zou, P. Yan, Surface modifications of a hyperperitectic Zn-10 wt% Cu alloy by pulsed electron beam treatment, Surf. Coatings Technol. 388 (2020) 125530, doi:10.1016/j.surfcoat.2020.125530.
[14] Y.F. Ivanov, V. Gromov, S.V. Konovalov, D.V. Zagulyaev, P.Semin Petrikova, Modification of structure and surface properties of hypoeutectic silumin by intense pulse electron beams, Prog. Phys. Met. 19 (2018) 195–222, doi:10.15407/ufm.19.02.195.
[15] Y.F. Ivanov, D.V Zaguliaev, A.M. Glezer, V.E. Gromov, A.A. Abaturova, A.A. Leonov, A.P. Semin, R.V Sundeev, Changes in surface structure and mechanical characteristics of Al–5 wt%Si alloy after irradiation by electron beam, Mater. Lett. 275 (2020) 128105, doi:10.1016/j.matlet.2020.128105.
[16] B. Gao, N. Xu, P. Xing, Shock wave induced nanocrystallization during the high current pulsed electron beam process and its effect on mechanical properties, Mater. Lett. 237 (2019) 180–184, doi:10.1016/j.matlet.2018.11.054.
[17] H. Yue, Y. Chen, X. Wang, F. Kong, Effect of beam current on microstructure, phase, grain characteristic and mechanical properties of Ti-47Al-2Cr-2Nb alloy fabricated by selective electron beam melting, J. Alloys Compd. 750 (2018) 617–625, doi:10.1016/j.jallcom.2018.03.343.
[18] Y.R. Liu, K.M. Zhang, J.X. Zou, D.K. Liu, T.C. Zhang, Effect of the high current pulsed electron beam treatment on the surface microstructure and corrosion resistance of a Mg-4Sm alloy, J. Alloys Compd. 741 (2018) 65–75, doi:10.1016/j.jallcom.2017.12.227.
[19] Y. Liu, K. Zhang, J. Zou, P. Yan, X. Zhang, L. Song, Microstructure and property modifications in surface layers of a Mg-4Sm-2Al-0.5Mn alloy induced by pulsed electron beam treatments, J. Magnes. Alloy. 9 (2021) 216–224, doi:10.1016/j.jma.2020.02.019.
[20] X.-T. Cao, J. Hu, W.-J. Huo, X.-C. Xi, W.-S. Zhao, Effects of Pseudo-spark Discharge Pulsed Electron Beam Irradiation on the Microstructure and Properties of 6061 Aluminum Alloy, Procedia CIRP 95 (2020) 954–959, doi:10.1016/j.procir.2020.03.148.
[21] Y. Hao, B. Gao, G.F. Tu, S.W. Li, C. Dong, Z.G. Zhang, Improved wear resistance of Al-15Si alloy with a high current pulsed electron beam treatment, Nucl. Instruments Methods Phys. Res. Sect. B Beam Interact. with Mater. Atoms. (2011), doi:10.1016/j.nimb.2011.04.010.
[22] B. Gao, Y. Hao, W.F. Zhuang, G.F. Tu, W.X. Shi, S.W. Li, S.Z. Hao, C. Dong, M.C. Li, Study on continuous solid solution of Al and Si elements of a high current pulsed electron beam treated hypereutectic Al17.5Si alloy, Phys. Procedia. 18 (2011) 187–192, doi:10.1016/j.phpro.2011.06.079.
[23] K. Zhang, J. Zou, T. Grosdidier, C. Dong, D. Yang, Improved pitting corrosion resistance of AISI 316L stainless steel treated by high current pulsed electron beam, Surf. Coatings Technol. 201 (2006) 1393–1400, doi:10.1016/j.surfcoat.2006.02.008.
[24] H. Xia, C. Zhang, P. Lv, J. Cai, Y. Jin, Q. Guan, Surface alloying of aluminum with molybdenum by high-current pulsed electron beam, Nucl. Instruments Methods Phys. Res. Sect. B Beam Interact. with Mater. Atoms. 416 (2018) 9–15, doi:10.1016/j.nimb.2017.11.028.
[25] C. Zhang, P. Lv, J. Cai, Y. Zhang, H. Xia, Q. Guan, Enhanced corrosion property of W-Al coatings fabricated on aluminum using surface alloying under high-current pulsed electron beam, J. Alloys Compd. 723 (2017) 258–265, doi:10.1016/j.jallcom.2017.06.189.
[26] S. Hao, M. Li, Producing nano-grained and Al-enriched surface microstructure on AZ91 magnesium alloy by high current pulsed electron beam treatment, Nucl. Instruments Methods Phys. Res. Sect. B Beam Interact. with Mater. Atoms. 375 (2016) 1–4, doi:10.1016/j.nimb.2016.03.035.
[27] M.C. Li, S.Z. Hao, H. Wen, R.F. Huang, Surface composite nanostructures of AZ91 magnesium alloy induced by high current pulsed electron beam treatment, Appl. Surf. Sci. 303 (2014) 350–353, doi:10.1016/j.apsusc.2014.03.004.
[28] H. Wang, S. Hao, Surface nanostructure and improved microhardness of 40CrNiMo7 steel induced by high current pulsed electron beam treatment, Nucl. Instruments Methods Phys. Res. Sect. B Beam Interact. with Mater. Atoms. 403 (2017) 45–50, doi:10.1016/j.nimb.2017.05.002.
[29] S. Kumar, S. Prakesh Tewari, U. Rajak, A. Dasore, T.N. Verma, Properties evaluation of A356 and A319 Aluminum alloys under different casting conditions, Mater, Today Proc. (2021), doi:10.1016/j.matpr.2021.03.492.
[30] E. Vandersluis, C. Ravindran, D. Sediako, A. Elsayed, G. Byczynski, Strontium-modification in the stepwise solidification of A319 Al alloy: An in-situ neutron diffraction study, J. Alloys Compd. 792 (2019) 240–249, doi:10.1016/j.jallcom.2019.04.037.
[31] N. Kesangam, S. Pinitsoontorn, S. Srimanosaowapak, Effect of initial microstructure on induction heating of A319 aluminium alloy, Mater. Today Proc. 5 (2018) 9615–9623, doi:10.1016/j.matpr.2017.10.148.
[32] F. Farhang Mehr, S. Cockcroft, C. Reilly, D. Maijer, Investigation of the efficacy of a water-cooled chill on enhancing heat transfer at the casting-chill interface in a sand-cast A319 engine block, J. Mater. Process. Technol. 286 (2020) 116789, doi:10.1016/j.jmatprotec.2020.116789.
[33] A. Lombardi, F. D'Elia, C. Ravindran, R. MacKay, Replication of engine block cylinder bridge microstructure and mechanical properties with lab scale 319 Al alloy billet castings, Mater. Charact. 87 (2014) 125–137, doi:10.1016/j.matchar.2013.11.006.
[34] K. Anderson, J. Weritz, J.G. Kaufman, eds., 319.0, A319.0, B319.0, and 320.0[1]: Al-Si-Cu General Purpose Foundry Alloys, Prop. Sel. Alum. Alloy. 2B (2019) 0. https://doi.org/ 10.31399/asm.hb.v02b.a0006562.
[35] ISO, International Standard ISO 6892-1 Metallic materials — Tensile testing 2009 (2009).
[36] I.Y. Zaguliaev D., Gromov V., Konovalov S., Electron-Ion-Plasma Modification of a Hypereutectic Al-Si Alloy (1st Edition), CRC Press, 2020. https://doi.org/https://doi.org /10.1201/9781003045960.
[37] A. V Tkachenko, E.A. Petrikova, Y.F. Ivanov, A.D. Teresov, Regularities of Structure and Phase Composition Formation of Surface Layer of Silumin Subjected to Electron-Beam Treatment, in: High Technol. Res. Appl. 2015, Trans Tech Publications Ltd, 2016: pp. 715–718. https://doi.org/ 10.4028/www.scientific.net/KEM.685.715.
[38] D. Zaguliaev, S. Konovalov, Y. Ivanov, V. Gromov, Effect of electron-plasma alloying on structure and mechanical properties of Al-Si alloy, Appl. Surf. Sci. 498 (2019) 143767, doi:10.1016/j.apsusc.2019.143767.
[39] B.J. Inkson, 2 - Scanning electron microscopy (SEM) and transmission electron microscopy (TEM) for materials characterization, in: G. Hübschen, I. Altpeter, R. Tschuncky, H.-G.B.T.-M.C.U.N.E. (NDE) M. Herrmann (Eds.), Woodhead Publishing, 2016: pp. 17–43. https://doi.org/https://doi.org/ 10.1016/B978-0-08-100040-3.00002-X.
[40] R.P. Ferrier, Interpretation of electron diffraction patterns, Non-Destructive Test 1 (1968) 184, doi:10.1016/S0029-1021(68)80015-5.